ACS APPLIED MATERIALS & INTERFACES

Surfaces, Interfaces, and Applications

Design of intense nanoscale stray fields and gradients at magnetic nanorod interfaces

Yurii P. Ivanov, Jonathan Leliaert, Adrian Crespo, Matteo Pancaldi, Christopher Tollan, Jurgen Kosel, Andrey Chuvilin, and Paolo Vavassori

ACS Appl. Mater. Interfaces, **Just Accepted Manuscript** • DOI: 10.1021/acsami.8b19873 • Publication Date (Web): 04 Jan 2019

ACS Publications

is published by the American Chemical Society. 1155 Sixteenth Street N.W., Washington, DC 20036

Design of intense nanoscale stray fields and gradients at magnetic nanorod interfaces

Yurii P. Ivanov[†,|,,‡], Jonathan Leliaert[§,‡], Adrian Crespo[‖], Matteo Pancaldi[‖], Christopher Tollan[‖], Jurgen Kosel[⊥], Andrey Chuvilin[‖,#], Paolo Vavassori[‖,#]*

[†] Department of Materials Science & Metallurgy, University of Cambridge, Cambridge CB3 0FS, UK

[|] School of Natural Sciences, Far Eastern Federal University, 690950, Vladivostok, Russia

[§] Dept. of Solid State Sciences, Ghent University, BE9000 Ghent, Belgium

[‖] CIC nanoGUNE Consolider, Av. de Tolosa 76, 20018, San Sebastian, Spain

[⊥] King Abdullah University of Science and Technology, Thuwal, 23955, Saudi Arabia

[#] IKERBASQUE, Basque Foundation for Science, Maria Diaz de Haro 3, 48013, Bilbao, Spain

KEYWORDS nanomagnets arrays, TEM, MOKE, micromagnetic simulations, patterned stray fields

ABSTRACT

We explore electrodeposited ordered arrays of Fe, Ni and Co nanorods embedded in anodic alumina membranes as a source of intense magnetic stray field gradients localized at the nanoscale. We perform a multiscale characterization of the stray fields using a combination of experimental methods (Magneto-optical Kerr effect, Virtual Bright Field Differential Phase Contrast Imaging) and micromagnetic simulations, and establish a clear correlation between the stray fields and the magnetic configurations of the nanorods. For uniformly magnetized Fe and Ni wires the field gradients vary following

saturation magnetization of corresponding metal and the diameter of the wires. In the case of Co nanorods, very localized (~10 nm) and intense (> 1T) stray field sources are associated with the cores of magnetic vortexes. Confinement of that strong field at extremely small dimensions leads to exceptionally high field gradients up to 10^8 T/m. These results demonstrate a clear path to design and fine-tune nanoscale magnetic stray field ordered patterns with a broad applicability in key nanotechnologies, such as nanomedicine, nanobiology, nanoplasmonics and sensors.

INTRODUCTION

Micro- and nanosized magnets are promising tools for manipulation,[1, 2] sorting, [3] and detection of biological samples,[3-5] or for applications in surface chemistry,[6] and sensor technologies.[7] A review of recent advances in this broad and emerging research topic can be found in Ref.[8] In the case of medicine and bio-chemistry applications, literature indicates that a fine control of both the gradient and the configuration of the magnetic stray field produced by arrays of nanomagnets is required. [9-10] One example, illustrating the potential of such substrates for bio-medical studies and applications, is that of an array of micron-sized Nd-Fe-B rods covered with parylene (poly(p-xylylene) polymer), utilized to study the effects of magnetic fields on the proliferation and differentiation of stem cells.[11] High magnetic field gradient causes the cells to attach themselves to and grow on the edges of the micromagnets. It was shown that high magnetic field gradients can assist and direct cell migration, thereby allowing one to build up tunable

interconnected stem cell networks - an elegant route for tissue engineering and regenerative medicine. The possibility of using nanomagnets with high stray field gradient in self-assembling process was further elaborated in several studies.[12-16] Thus in Ref.[16] the authors investigated the assembly of magnetotactic bacteria and magnetite or cobaltite nanoparticles on micron-sized periodic patterns of commercial audio tapes. Local magnetic field gradients also find use in surface chemistry for controlling the position of adsorption of diamagnetic molecules.[6] These real-life applications call for an affordable and scalable fabrication process of large area nanomagnetic substrates with tunable stray field configuration and gradient.

Commonly, arrays of nano-magnets on surfaces are produced by lithography process,[17-19] which is time consuming, expensive and is limited in spatial resolution. An alternative method to generate surface stray fields is by arrays of magnetic nanorods embedded in a non-magnetic template,[20] provided that the magnetic properties and thus the stray fields generated by these arrays can be controlled. Electrodeposition in templates is an inexpensive and fast technology to produce arrays of very thin (<100 nm) nanorods of arbitrary large area. The magnetic properties of such arrays can be manipulated by varying the material composition or crystal structure,[20-23] and their use has already been demonstrated in stem cells analysis,[24] pressure sensors,[25] and 3D memory devices.[26-27]

Besides stray fields design, the other challenge lays in the deficiency of characterization techniques for magnetic stray fields at the nanoscale. Besides the recent progress in the quantitative measurement of magnetic field by magnetic force microscopy (MFM),[28] scanning magnetoresistance (MR) microscopy,[29] scanning hall probe microscopy (SHPM)[30] and the Nitrogen Vacancy (NV) center-based technique,[31] the spatial resolution offered by these methods is still limited to 50-100 nm. In the case of MFM, the magnetic tip-sample interaction is also an

issue. Transmission Electron Microscopy (TEM) based methods as, e.g., off-axis electron holography, have the required spatial resolution, although they entail complications related to the complex sample preparation and to the very limited field of view. Indeed, most of the TEM studies were focused on the investigation of the magnetic structure and stray fields of individual nanorods by electron holography.[32-37] An attempt to apply the electron holography for measuring the magnetic state of an array of Ni nanowires was reported in Ref.[38]

METHODS

Here we approach the challenge of imaging surface stray fields in profile view by using Virtual Bright Field Differential Phase Contrast (VBF-DPC) method[39] and combine this method with the magneto-optical Kerr effect (MOKE) magnetometry and micromagnetic simulations. Initially, we magnetically characterize the substrates using MOKE[40] to perform vector magnetometry[41] and to record longitudinal and polar hysteresis loops. Although MOKE can be implemented to achieve a sub-micron spatial resolution,[42-43] this would still be insufficient to study individually the small nanorods investigated here. To gain insights in the magnetic configuration inside the nanorod arrays, we complemented the experimental results with micromagnetic simulations aiming at reproducing longitudinal and polar MOKE loops simultaneously. A portion of each substrate is taken to determine precisely the size, shape, array symmetry and order, and crystal structure of the nanorods using high resolution TEM. This information provides key hints about magneto-crystalline and shape anisotropies, and geometrical arrangement, which are utilized to compute hysteresis loops using advanced micromagnetic simulations. This information allows to reduce the number of free adjustable parameters and thus the number of magnetic configurations that can arise inside nanorods in simulations, which target on agreement of *both* polar and longitudinal experimental magnetization loops. Achieving this agreement gives unique remanent

magnetic configuration, given the constraints dictated by material magnetization, size and shape of the rod, and crystal structure. This approach enables to connect local magnetization states in an individual rod with the macroscopically produced stray field pattern from the nanorods array. To perform a truly nanoscale magnetic characterization of the stray field generated by the nanorods and thus to confirm micromagnetic simulation results, we complement the vector MOKE study by the recently developed TEM-based technique - VBF-DPC, which is able to spatially discern and quantify magnetic fields with nanometre resolution over a field of view as large as 100 μm.[39] VBF-DPC method is the original modification of the conventional Differential Phase Contrast imaging in STEM mode allowing for this kind of study in any type of TEM with scanning capability. The detailed description of the method together with the approach to quantify the nanoscale magnetic field can be found in Ref.[39] There we demonstrated the very high spatial resolution of the VBF DPC method (around 4 nm) and its high sensitivity to magnetic fields (the signal measured could be better than 0.01 T depends on the experimental conditions).

We have investigated arrays of nanorods consisting of bcc Fe, fcc Ni and hcp Co, which have been produced by electrodeposition inside anodic alumina membranes (AAMs) with self-assembled nanopores ordered in a hexagonal pattern. The AAMs have been prepared by a two-step anodization process in oxalic acid, tuned to produce a hexagonal array of pores with a diameter of about 40 nm. Next, the non-oxidized Al layer at the bottom of the substrate, as well as the alumina bottom layer, has been chemically removed. A thin Au layer has then been sputtered onto the open backside of the membrane to serve as an electrode for the subsequent electroplating of either, hcp Co,[22,44] fcc Ni[26] or bcc Fe.[21,45] The details of the electrodeposition are provided in Supporting Information. The electroplating time has been adjusted to reach

nanorods length of around 20 μm. The samples have been further polished to remove the top part of the membrane, not containing nanorods, and to achieve a very smooth surface. The AAMs have been polished with a series of diamond abrasive films with decreasing grain sizes down to 0.1 μm. The final polishing step has been performed using a silica solution with particle sizes in the 20-50 nm range. The high surface quality of the polished membranes is proved by optical diffraction and SEM studies. Figure 1a depicts a Scanning Electron Microscopy (SEM) image of the surface of the final membrane with Ni nanorods array. The SEM micrograph shows that the nanorods have a highly ordered hexagonal arrangement within areas ("crystallites") of up to a few μm^2 in size. Crystallites of different orientations are marked by coloured areas in Figure 1a for illustration. The average diameter of the nanorods and the distance between centers, extracted from the SEM micrographs, are 50 nm and 100 nm, respectively. Using a 2D fast Fourier transform (FFT) analysis of the SEM micrograph, the high order of the hexagonal arrangement of the nanorods within individual crystallites can be appreciated, as shown in Figure 1c, which can be compared to the 2D-FFT analysis of the whole image (Figure 1b) displaying rings rather than individual spots due to different orientation of various crystallites.

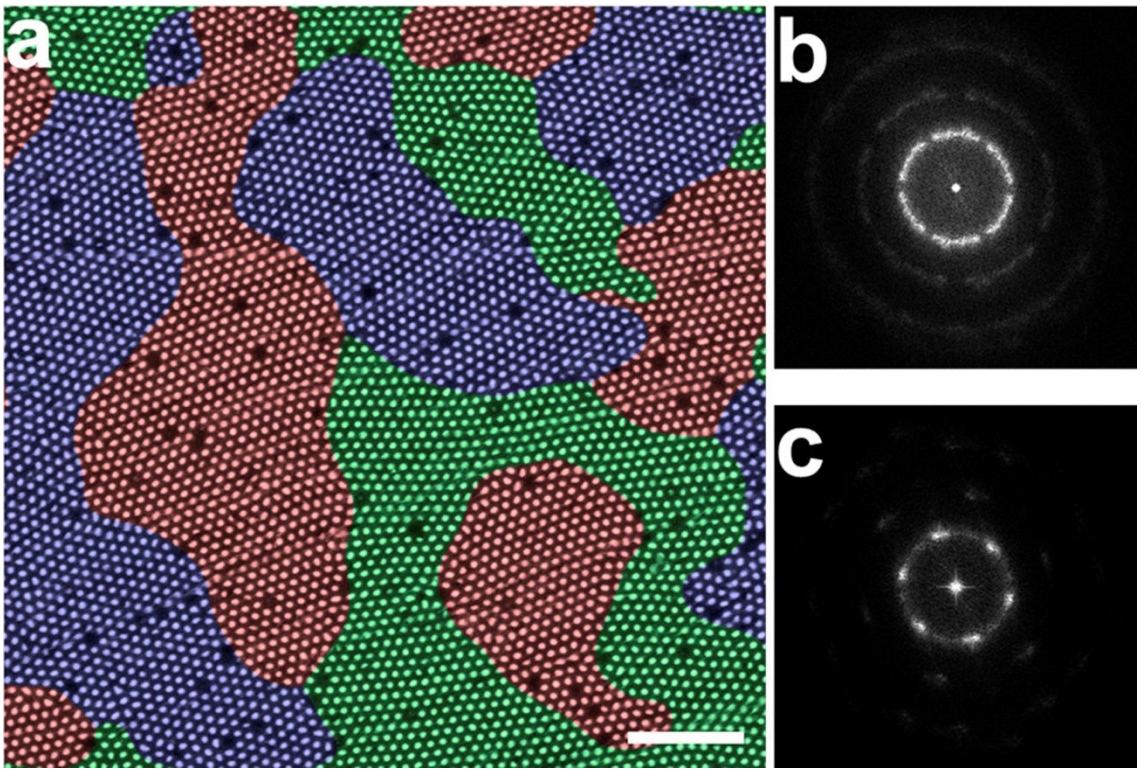

Figure 1. a SEM image of a polished alumina membrane with embedded nanorods. The colored areas are examples of "crystallites" with different orientations, i.e., ordered regions with highly ordered hexagonal arrangement of the nanorods. Panel **b** shows a 2D FFT analysis of the whole image and **c** represents one of an individual crystallite. The latter shows 6-fold symmetry, which confirms hexagonal arrangement in individual crystallites, while the upper pattern shows a rings-like pattern due to different orientation of the crystallites. The scale bar in panel **a** is 1 μm.

For the VBF-DPC characterization in TEM, cross-sectional lamellas for each sample have been prepared using focused ion beam (FIB). The standard FIB TEM lamellae preparation technique[46] requires deposition of a Pt protection layer on the surface, which would hinder the observation of the stray fields. In order to protect the surface during the FIB process avoiding the deposition of the Pt layer, we have instead used a ~500 nm thick self-supporting diamond film as a protecting cover, which was removed at the final step of the lamella preparation. Thus, the top surface of the prepared sample was not damaged during FIB milling. Final FIB polishing was conducted at a reduced voltage of 2 kV to further thin and minimize the amount of damage and reduce levels of implanted Ga in the sides of the final specimen. The lamellae have purposely been made thick - about 450 nm, corresponding to ~4 periods of the hexagonal AAM pore pattern. Figure 2 shows the side and top views of thus prepared lamella, clearly illustrating an opened and undamaged surface of the AAM.

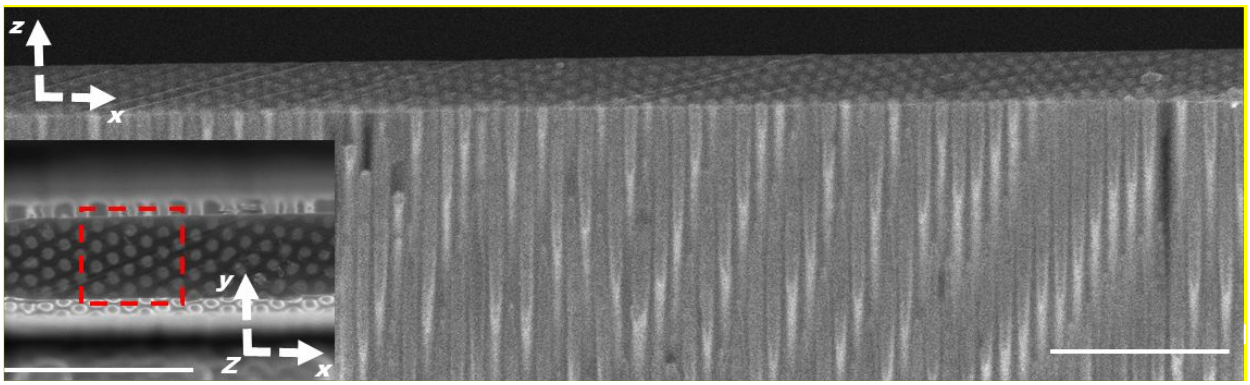

Figure 2. Side and the top views of the FIB lamella of nanorods array inside the AAM used for TEM investigations. The red dashed rectangle shows a typical area of the array used for the reconstruction of the magnetic stray field and corresponds also to the unit

cell used in the micromagnetic simulations. The scale bar in panel **a** is 1 μm. The arrows indicate view directions.

RESULTS AND DISCUSSION

The measured polar and longitudinal MOKE hysteresis loops are shown in Figure 3 (symbols).

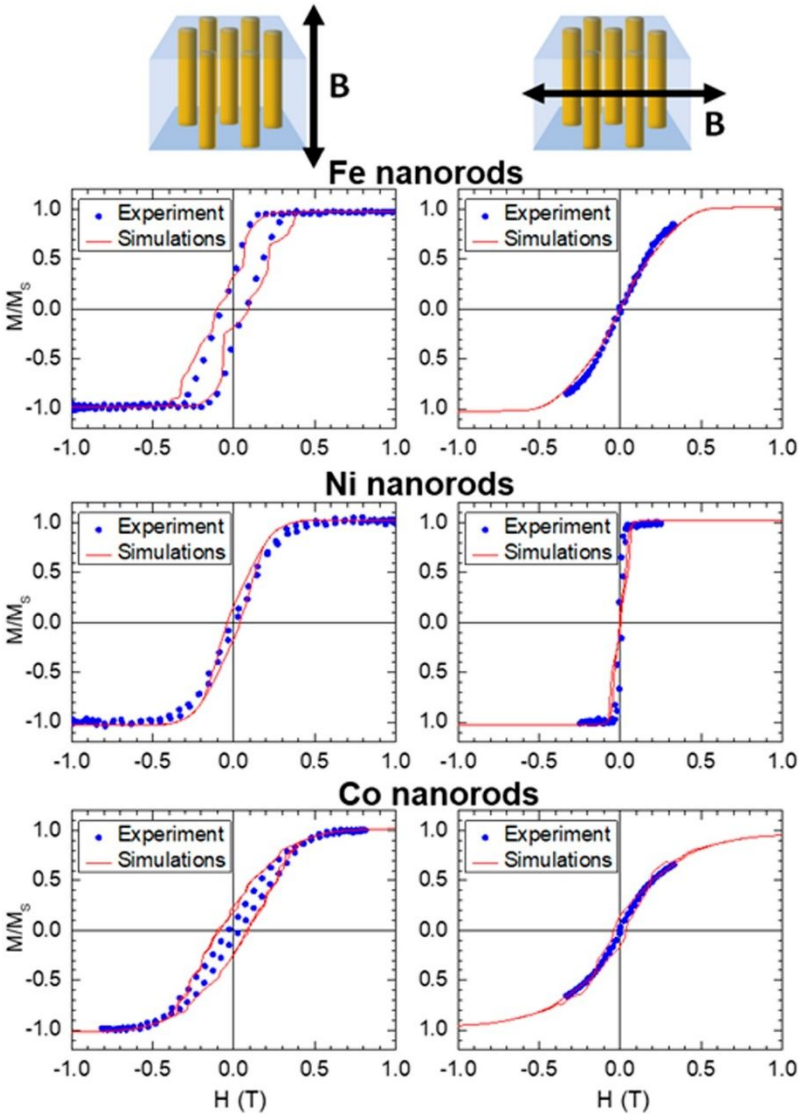

Figure 3. MOKE loops, normalized to the saturation magnetization, from Fe, Ni and Co nanorod arrays. Schematics on top show the magnetic field configuration during the experiments (polar, left column; longitudinal, right column). Blue dots correspond to the experimental results, while the red curves show the results of micromagnetic simulations.

To gain insights in the magnetic configuration inside the nanorod arrays, we complemented the experimental results with micromagnetic simulations using mumax[3].[47-48] The simulated geometry consisted of 21 nanorods, each 700 nm long and 50 nm in diameter, placed on a hexagonal lattice with the distance between rods being 100 nm. This geometry was discretized in 128 x 128 x 256 finite difference cells of 2.70 x 3.13 x 2.73 nm^3, comparable to the exchange length of Ni (4.7 nm), Co (2.6 nm), and Fe (4.4 nm). Using periodic boundary conditions, the array unit cell of 346 nm by 400 nm was repeated 5 times in the AAM plane to arrive at an average "crystallite" size of approximately 2 μm by 2 μm in agreement with the sizes determined from SEM micrographs of the membranes (see Figure 2). The nanorod length of 700 nm corresponds to the average thickness of the lamella used for TEM investigations and reproduces the conditions of the MOKE experiments. It has been verified that a further increase of the length of the nanorods does not affect the obtained hysteresis loops. Each nanorod was simulated with a single crystal structure, but the directions of the cubic (Fe and Ni) and uniaxial (for Co) magnetocrystalline anisotropy axes were varied randomly from nanorod to nanorod to simulate a realistic sample. The anisotropy constants K and exchange stiffness A were both equal to the tabulated values for the bulk materials, i.e. $K = 48 \times 10^3$ J/m^3 and $A = 2.1 \times 10^{-11}$ J/m for Fe,[49] $K = 450 \times 10^3$ J/m^3 and A

= 1.3×10^{-11} J/m for Co,[50] and K = -4.8×10^3 J/m^3 and A = 3.4×10^{-12} J/m for Ni.[51] It is known that the stresses induced by the AAM can introduce significant effect on the magnetic properties of Ni nanowires embedded into AAM matrix due to the negative magnetostriction of fcc Ni.[52-53] Indeed, to reproduce the experimental results the magnetostriction of the Ni nanorods was taken into account by a uniaxial hard axis along the length direction of the rods with an anisotropy constant uniformly distributed between -25 and -100 kJ/m^3. The saturation magnetization (M_S) values used in the simulations were 1200×10^3 A/m, 1760×10^3 A/m, and 490×10^3 A/m for Fe, Co, and Ni, respectively. For Co and Ni, these values correspond the tabulated values for bulk material, while in the case of Fe M_S needed to be reduced by a 30% as compared to bulk bcc Fe (1700×10^3 A/m) in the topmost 50 nm of the nanorod, in order to reproduce the measured MOKE results. This reduction is justified by considering that MOKE is only sensitive to the surface up to a depth of approximately of 50 nm, and the fact that surface oxidation in Fe samples is typically much stronger than for Co and Ni ones. Typically, the natural oxidation layer for the nanorods released from the AAM is about few nanometres (see Supporting Information). This layer acts as a protection layer for further oxidation of Co and Ni nanorods. In contrast, our previous study[21] demonstrated the strong oxidation of the polycrystalline Fe nanorods exposed to the air, the resulted magnetite shell has a magnetisation 5 times less than the Fe. Thus, it was reasonable to assume the reduced magnetisation value for the tip of the Fe nanorod. Using the freedom of micromagnetic simulations, we also investigated the robustness of our results towards thermal fluctuations,[54] disorder and imperfections, using realistic estimates of their strength.[55] In particular, we have varied the material parameters, the easy axes directions, the nanorod shape, diameter, distance and the regularity of their grid. Furthermore, we have included pinning centers in the nanorods, and investigated the effect of misalignments of the

sample with respect to the polar or longitudinal applied external fields. We conclude that both the observed magnetization states and the similarity from one calculated MOKE loop to the next are robust against these sources of disorder.

The comparison between the experimental and simulated MOKE results for each array displayed in Figure 3 shows a good agreement. Fig. 4 shows the magnetic configuration at remanence close to the top of the nanorods for Co, Ni and Fe, as calculated with mumax[3], showing a uniform magnetization for the Fe and Ni nanorods and a vortex structure for the Co nanorod.

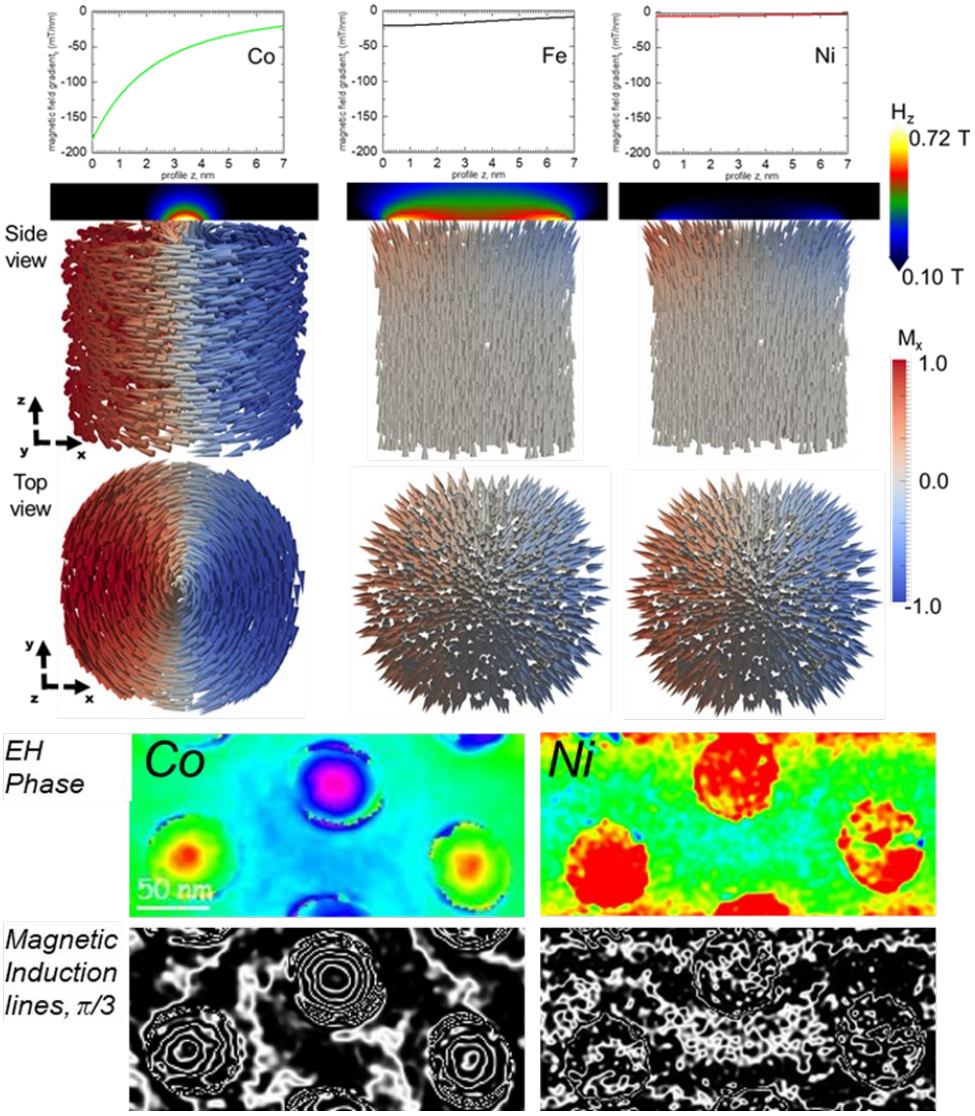

Figure 4. Magnetic configuration at remanence close-up of the top of the nanorods for Co, Ni and Fe, as calculated with mumax[3], showing a uniform magnetization for the Fe and Ni nanorods and a vortex structure for the Co nanorod. The small arrows and colors indicate the magnetization direction: white corresponds to an out-of-plane magnetization (along the length of the nanorods), while the red/blue color corresponds to the "vertical" in-plane direction. Above the nanopillars a cross section of the magnetostatic field is shown. The graphs present the magnetic field gradient at the center of nanopillars in the direction parallel to the pillar axis, clearly showing the large field gradients associated with the vortex cores. At the bottom the reconstructed phase and magnetic induction lines from EH study of the Co and Ni nanorods in-plane of AAM are shown.

To confirm the two aforementioned magnetic structures for different nanorods, we performed the off-axis Electron Holography (EH) study of the remnant state of the Co and Ni nanorod arrays in-plane of the AAM. The details of the EH study are shown in Figure 4 for the case of Co and Ni nanorod arrays. It is clearly observed the vortex state for Co nanorods and the absence of the magnetic signal in-plane of the AAM for Ni nanorods which confirmed the formation of the single domain state with magnetization oriented normal to the AAM surface.

The magnetic configuration of an individual nanorod inside AAMs is primarily determined by the material magnetic properties, the nanorod size and shape, and the crystalline structure chosen

for the electrodeposition. Typically, the magnetic nanorods are polycrystalline, with a largely dominant out-of-plane magnetic easy axis with respect to the AAM due to the shape anisotropy of the nanorods.[20,56] In this situation, the observed uniform out-of-plane magnetization for Fe and Ni, is corroborated by an analysis of the relevant micromagnetic energy terms, i.e. the anisotropy energy, the exchange energy and the magnetostatic energy. Because we are considering an easy axis in the out-of-plane direction, the large shape anisotropy energy due to the high aspect ratio of the nanorod favours the magnetization to lie in this direction as well. The exchange interaction does not have a preferential direction, but prefers a uniform magnetization state. A more interesting situation, however, arises when the nanorods are deposited as a single crystal structure with strong magnetocrystalline anisotropy away from the out-of-plane direction. This situation is achieved in the case of single crystal Co nanorods grown with a hcp structure and the c-axis (which corresponds to a uniaxial magnetocrystalline easy axis) oriented in the plane of the AAM,[57] leading to a strong magnetocrystalline anisotropy perpendicular to the shape anisotropy. The resulting competition between the two anisotropies gives rise to a frustrated and rich magnetic behaviour. In particular, it may lead to three different possible remanent magnetization states: a uniform out-of-plane magnetization, as for Fe and Ni nanorods, if the shape anisotropy is dominant, a uniform in-plane magnetization if the magnetocrystalline anisotropy dominates, or a complex 3D vortex structure consisting of an out-of-plane magnetized vortex core surrounded by a whirling magnetization lying in a plane perpendicular to the rod axis.[22,57] Which state will be realized depends on the complex interplay between the micromagnetic energy terms.[58] A first evaluation of the relative strength of shape and magnetocrystalline anisotropies for our Co nanorods shows that magnetocrystalline term is higher that the shape one but not as much as to achieve a uniform in-plane magnetization, that can thus be excluded. The choice of the nanorod

between the other two possibilities, vortex and uniform out-of-plane magnetization, is then involving also the exchange energy contribution. The exchange energy favours the uniform magnetization, thereby the nucleation of a vortex state occurs at an extra energy cost that depends on its radius. For nanorods with large radius, i.e., 100 nm and higher, the vortex state is always preferential as the exchange energy only grows as the logarithm of the radius, while the anisotropy energy grows quadratically. The smallest radius at which a vortex state will be found is however difficult to estimate because as the radius reduces below 100 nm the energy contribution of the vortex core, whose diameter is in the order of 10 nm in the present case, so far neglected has to be considered. The additional energy cost of the vortex core, which has a complex profile determined by the interplay between all energy terms, is difficult to describe in an analytic form and only micromagnetic simulations could confirm that the vortex state is indeed favoured in our Co nanorods.

Fig. 4 shows also the calculation of the stray field generated by each type of nanorod (topmost panels)**.** The plots present the magnetic field gradient at the center of nanopillars in the direction parallel to the pillar axis (z-axis) clearly showing a much larger field gradient associated with the vortex core formed by Co nanorod. The stray field originates primarily from those surfaces of the nanorod at which the magnetization is forming an angle different from $\pi/2$ with the out-going surface normal, namely where $\mathbf{M \cdot n}$ is different from zero. In the case of our nanorods these are located the top and bottom surfaces. In addition, the field strength depends on the extension of the surface where $\mathbf{M \cdot n}$ is non-zero: the smaller the extension the stronger the stray field and even much stronger the field gradient. This last consideration makes Co nanorods particularly interesting since this region of non-zero $\mathbf{M \cdot n}$ is limited to the vortex core extension that is substantially smaller than that of the entire top/bottom surface of the nanorods as in the case of

Fe and Ni. In summary, for uniform out-of-plane magnetization (Fe and Ni), the stray fields have a similar profile, although the intensity is stronger for Fe as it has a much larger saturation magnetization. In the Co nanorods array, as compared to the other two cases, the stray field is compressed to the size of the vortex core and the out-of-plane component H_z displays a strong maximum close to the nanorod centre, which is substantially smaller than the nanorod diameter. Therefore, although Co has a saturation magnetization that is slightly lower than that of Fe, the stray field generated by Co nanorods is expected to be higher and, more importantly, with a field gradient that should be much higher. This makes Co nanorods a promising candidate for applications requiring dense ordered arrays with a very local concentration of the out-of-plane flux. We note here that Co nanorods can display multi-vortices states. This can be understood considering that when reducing the externally applied field from saturation, vortices nucleate at the nanorod top and bottom edges, and they might have a different chirality. When this happens, the remanent state is a double vortex structure with a transition in the middle of the nanorod, but this slightly more complex state does not have an influence on the stray fields at the nanorod ends.

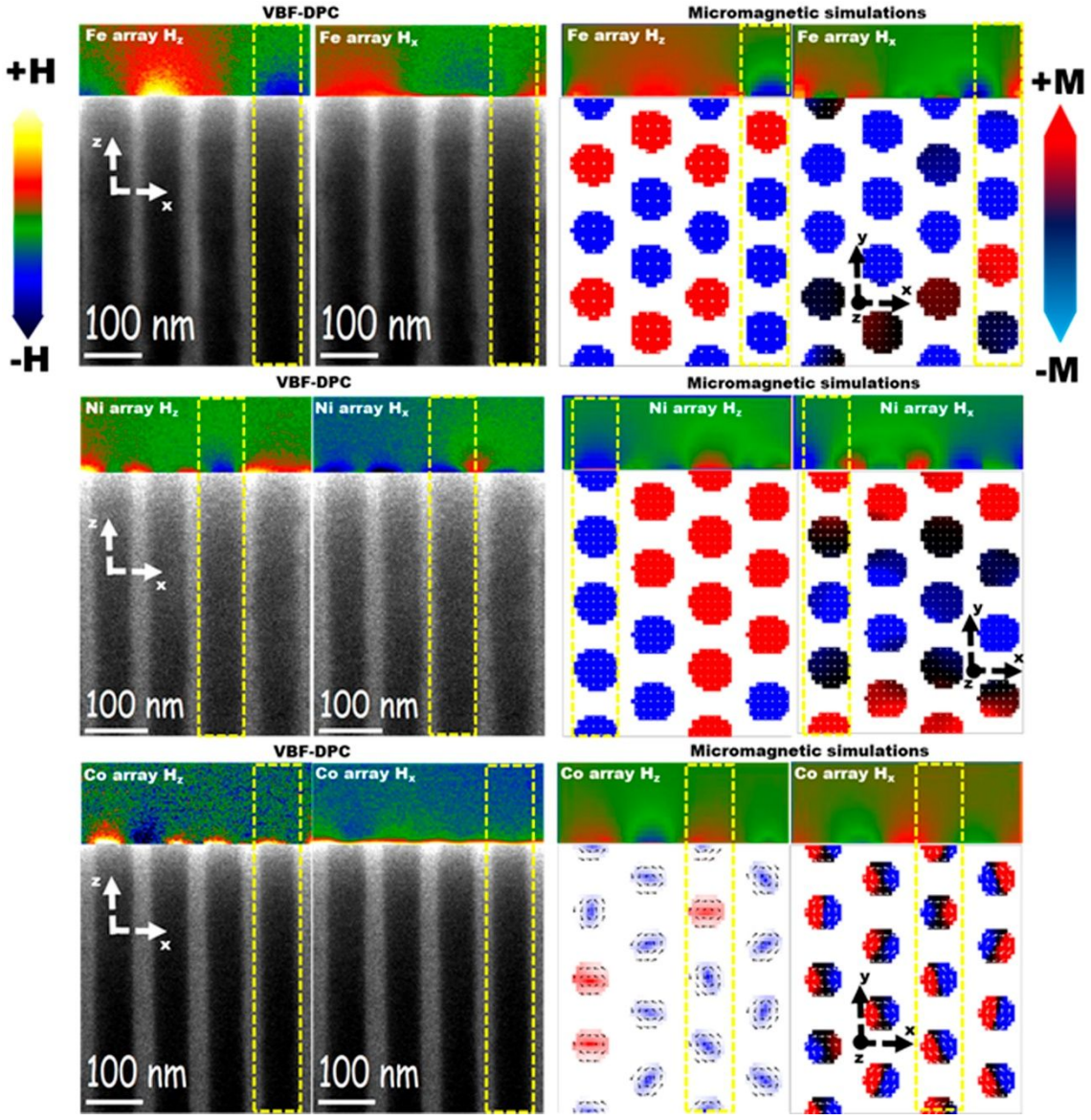

Figure 5. Top part of figures: two orthogonal components (Hz and Hx) of the stray fields measured by VBF-DPC and simulated for Ni, Fe and Co nanorod arrays. The dashed rectangles show examples of good fits between the experimental and numerical data. The bottom part of the experimental data depicts the BF STEM image of the array area, while the bottom part of the simulation results shows a top view of the magnetization

structure on the nanorod edges Note that the bottom part of the figures thus show data with a different orientation.

For an individual Fe or Ni nanorod with high aspect ratio, the remanent state after polar saturation is a uniform configuration with the magnetization aligned along the nanorod length axis due to the shape anisotropy. Despite the uniform magnetization of each individual nanorods, the observed remanent magnetizations are significantly lower than 1. This observation can be explained again by micromagnetic simulations. The right panels of Figure 5 display the magnetization arrangement in the unit cell used in the micromagnetic simulations. As depicted in the panels, the strong magnetostatic interaction between the close-packed nanorods of Fe and Ni comprising the hexagonal network gives rise to an uncompensated long-range anti-ferromagnetic order. Indeed, as shown in the top and middle panels of Figure 5 (panels showing simulated component of magnetisation M_Z of nanorods), at remanence the magnetization in some nanorods has switched to the other side (-z) with respect to the direction of the applied field (+z). The resulting magnetic configuration inside a crystallite thus consists of nanorods, either isolated or bundled in groups of different size, in which the magnetization is pointing either upwards or downwards, thus explaining the reduced remanent magnetization that is observed in the experiment. In the simulated loop, shown in Figure 3, the Fe nanorods magnetization reduces in discrete steps as the magnetic field is reduced, corresponding to the switching of individual or small groups of nanorods. In our vector MOKE experiments, however, the measurement is over a large ensemble of crystallites, thereby the steps are smeared out giving rise to a smooth hysteresis curve. For a Fe array, the simulations predict that the number of unswitched nanorods

is larger than the number of switched ones. The remanent magnetization is thus expected to be larger than in the Ni array, where the number of switched and unswitched nanorods is almost the same, leading to the state with a very small remanence, as confirmed by the experimental polar loops. This difference can be easily understood considering that the saturation magnetization of Fe is approximately three times larger than for Ni and therefore leads to stronger shape anisotropy stabilizing the magnetic moment of the nanowires against the antiferromagnetically aligning dipolar interactions. Although a remanent state in which all the nanorods are magnetized along the same direction is not relevant for the applications addressed in this paper, it is clear that if such global configuration were needed it could be achieved simply by increasing the separation distance between the nanorods. This gives rise to another tuning parameter – the lattice spacing – to customize the stray field landscapes, by reducing the inter-rods magnetostatic dipolar interaction,

The results of the comparative analysis between MOKE experiments and micromagnetic simulations were further corroborated by detailed VBF-DPC investigations of the stray field produced by the three samples in their remanent state. The DPC maps of the stray fields for Ni, Fe and Co nanorod arrays are shown in the left panel of the Figure 5. DPC allows capturing two orthogonal components of the magnetic fields independently. For the Fe and Ni arrays, the out-of-plane component H_z (perpendicular to the surface of the substrate) is much stronger than the in-plane component and varies depending on the magnetic configuration in each nanorod. The maps for Fe and Ni are compatible with array of nanorods in a single domain state with magnetisation aligned in z direction (parallel to the nanorod axis). Figure 5 also shows the H_z and H_x components of the stray fields calculated from simulation results corresponding to the experimental observations (H_z and H_x extracted from VBF-DPC study) (left). The areas

displaying the best quantitative fit of experimental data to the micromagnetic simulations are indicated by dashed yellow rectangles.

Figure 6 shows the profiles of out of plane (H_Z) component as function of the distance from the AAM surface (z-axis) of the magnetic stray field generated by the nanorods, measured along the axis of the Fe, Ni and Co nanorods by VBF-DPC (see Figure 5). Indeed, in the case of Co, the rapid decay of the stray field emanating from the vortex core in close proximity of the surface, gives rise to a large field gradient in the order of 10^6-10^7 T/m in a region within 15 nm from the AAM surface. This is due to the small size of the vortex core diameter, which is in the order of the exchange length, i.e. for Co ~4 nm. In the case of Fe and Ni, the stray field decay is slower and the field gradient is about 10 times smaller in respect to Co, although the field reaches out to larger distances, 100-150 nm, from the AAM surface. It is important to note that the maximum field determined by VBF-DPC is underestimating the actual maximum value of the fields due to averaging caused by the limited DPC resolution (about 4 nm) and thickness of the sample consisting of the 4 nanorods in the row. In fact, it is clearly seen from the simulation results of individual nanorods shown on the Fig. 3. The value of the magnetic field gradient extracted close to the centre of the nanorod could reach 10^8 T/m in the case of the magnetic vortex of Co nanorod. As clearly seen from the experimental profiles on the Figure 6a the noise level is less than 0.01 T. This is the uncertainty of the measured stray field in the present case. The micromagnetic configuration at the remanence was used to calculate the stray fields. To reproduce the experimental data, the values of the entire array were projected on the xz plane with the discretization corresponded to the spatial resolution of the experimental data (6 nm).

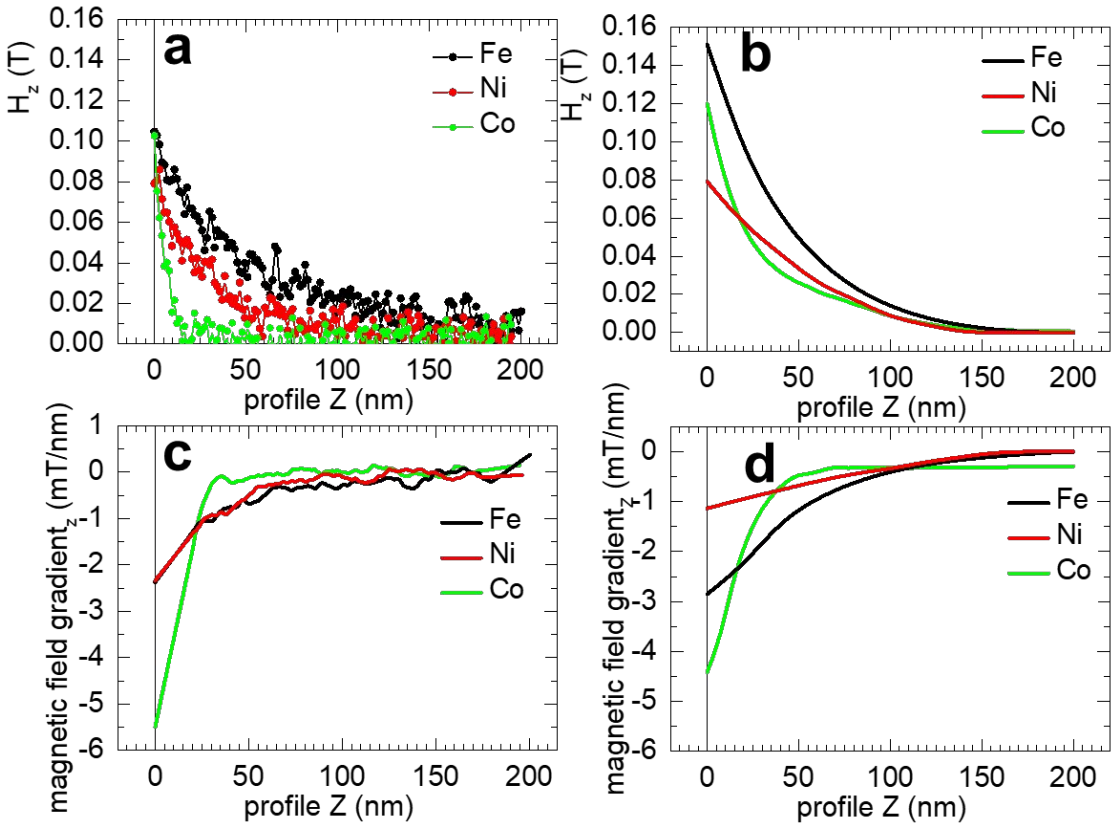

Figure 6. The profile of the Hz component of the magnetic field along the axis of the nanorods (z-axis) and magnetic field gradient **a, c** measured from the AAM surface by VBF-DPC for the Fe, Ni and Co nanorods and **b, d** extracted from micromagnetic simulation. It was calculated averaging over 2x64x2 cells in order to reproduce the experimental conditions.

CONCLUSIONS

Ordered nanorod arrays in AAMs with a hexagonal lattice are promising platforms for generating stray field patterns that can be useful for various applications like nanomedicine,

nanoplasmonics and sensors. We show that the magnetic stray field gradient can be investigated by combining MOKE and TEM-based DPC methods together with micromagnetic simulations, since this combination allows visualizing and quantifying highly localized stray fields of the studied Fe, Co and Ni nanorod arrays.

Our results show that AAMs with Fe nanorods exhibit the highest magnetic stray fields with the largest field range outside of the AAMs, while single crystal Co nanorods with their hcp c-axis oriented in the plane perpendicular to the nanorods long axes (i.e., lying in the AAM plane) provide a particularly large magnetic field gradient. The latter originates in a magnetic vortex structure, which is stabilized in this configuration due to a frustrated interaction between the magnetocrystalline and shape anisotropy, and contrasts the nearly uniform magnetic configuration that is found in the Fe and Ni nanorods.

We demonstrated that by varying the materials used, it is possible to design and fine-tune magnetic stray field patterns in the nanometer range over areas of several centimetres in size, even with very large magnetic field gradients resulting from intense local (only a few nm) field sources such as vortex cores.

As an example of application, for beads trapping, forces of tens and hundreds pN are needed to overcome drag forces in microfluidics. Forces depend on the gradient of field and magnetic susceptibility of the bead (Refs. 4 and 6) and if one wants to trap very small particles, 10 nm beads for instance, one needs a field gradient like that generated by our membranes, which is much larger than that achievable with lithographed structures.

ASSOCIATED CONTENT

Supporting Information. We provide additional information and figures on the preparation of the samples, the crystal structure characterization, the off-axis electron holography study, the details of the VBF-DPC method and the study of the natural oxidation of the nanorods (PDF).

AUTHOR INFORMATION

Corresponding Author

* Correspondence and requests for materials should be addressed to Dr. Yurii P. Ivanov, e-mail: ivanov.yup@gmail.com

Author Contributions

Y. I., A. Ch. and P. V. conceived the project, Y. I. and A. Ch. designed and performed TEM experiments and data analysis, P. V. and M. P. performed MOKE experiments and data analysis, J. L. and A. C. performed micromagnetic simulations, C. T. and J. K.

supported the experiments. All authors contributed to the manuscript writing. ‡These authors contributed equally.

ACKNOWLEDGMENT

P.V., A.Ch., and M.P. acknowledge support from the Spanish Ministry of Economy, Industry and Competitiveness under the Maria de Maeztu Units of Excellence Programme - MDM-2016-0618, the Project FIS2015-64519-R, and (M.P.) the grant BES-2013-063690. J.L gratefully acknowledges postdoctoral research fellowships by the Fonds Wetenschappelijk Onderzoek (FWO-Vlaanderen) and the Ghent University Special Research Fund (BOF). We gratefully acknowledge the support of NVIDIA Corporation with the donation of the GPU's used for this research. Y.P.I. acknowledge support from the grant 3.7383.2017/8.9 of Ministry of Education and Science of Russian Federation.

REFERENCES

[1] Donolato, M.; Vavassori, P.; Gobbi, M.; Deryabina, M.; Hansen, M. F.; Metlushko, V.; Ilic, B.; Cantoni, M.; Petti, D.; Brivio S.; Bertacco, R. On-Chip Manipulation of Protein-Coated Magnetic Beads via Domain-Wall Conduits. *Advanced Materials* **2010**, *22*, 2706-2716.

[2] Sarella, A.; Torti, A.; Donolato, M.; Pancaldi, M.; Vavassori, P. Two-Dimensional Programmable Manipulation of Magnetic Nanoparticles on-Chip. *Advanced Materials* **2014**, *26*, 2384-2390.

[3] Torti, A.; Mondiali, V.; Cattoni, A.; Donolato, M.; Albisetti, E.; Haghiri-Gosnet, A. M.; Vavassori, P.; Bertacco, R. Single Particle Demultiplexer Based on Domain Wall Conduits. *Appl. Phys. Lett.* **2012**, *101*, 142405.

[4] Vavassori, P.; Metlushko, V.; Ilic, B.; Gobbi, M.; Donolato, M.; Cantoni, M.; Bertacco, R. Domain Wall Displacement in Py Square Ring for Single Nanometric Magnetic Bead Detection. *Appl. Phys. Lett.* **2008**, *93*, 203502.

[5] Donolato, M.; Gobbi, M.; Vavassori, P.; Leone, M.; Cantoni, M.; Metlushko, V.; Ilic, B.; Zhang, M.; Wang, S. X.; Bertacco, R. Nanosized Corners for Trapping and Detecting Magnetic Nanoparticles. *Nanotechnology* **2009**, *20*, 385501.

[6] Ahrend, F.; Glebe, U.; Arnadottir, L.; Baio, J. E.; Fischer, D. A.; Jaye, C.; Leung, B. O.; Hitchcock, A. P.; Weidner, T.; Siemeling, U.; Ehresmann, A. Magnetic Field Landscapes Guiding the Chemisorption of Diamagnetic Molecules. *Langmuir* **2016**, *32*, 10491-10496.

[7] Alfadhel, A.; Kosel, J. Magnetic Nanocomposite Cilia Tactile Sensor. *Advanced Materials* **2015**, *27*, 7888-7892.

[8] Lim, B.; Vavassori, P.; Sooryakumar, R.; Kim, C. Nano/Micro-Scale Magnetophoretic Devices for Biomedical Applications. *J. Phys. D: Appl. Phys.* **2017**, *50*, 033002.

[9] Shapiro, B.; Kulkarni, S.; Nacev, A.; Sarwar, A.; Preciado, D.; Depireux, D. A. Shaping Magnetic Fields to Direct Therapy to Ears and Eyes. *Annu. Rev. Biomed. Eng.* **2014**. *16*, 455-481.

[10] Chung, H. J.; Castro, C. M.; Im, H.; Lee, H.; Weissleder, R. A Magneto-DNA Nanoparticle System for Target Specific Bacterial Identification. *Nat. Nanotechnol.* **2013**, *8*, 369-375.

[11] Zablotskii, V.; Dejneka, A.; Kubinova, S.; Le-Roy, D.; Dumas-Bouchiat, F.; Givord, D.; Dempsey, N. M.; Sykova, E. Life on Magnets: Stem Cell Networking on Micro-Magnet Arrays. *PLoS One* **2013**. *8*, e70416.

[12] Bidan, C. M.; Fratzl, M.; Coullomb, A.; Moreau, P.; Lombard, A. H.; Wang, I.; Balland, M.; Boudou, T.; Dempsey, N. M.; Devillers, T.; Dupont, A. Magneto-Active Substrates for Local Mechanical Stimulation of Living Cells. *Sci. Rep.* **2018**. *8*, 1464.

[13] Le Roy, D.; Shaw, G.; Haettel, R.; Hasselbach, K.; Dumas-Bouchiat, F.; Givord, D.; Dempsey, N. M. Fabrication and Characterization of Polymer Membranes with Integrated Arrays of High Performance Micro-magnets. *Mater. Today Commun.* **2016**. *6*, 50-55.

[14] Zanini, L. F.; Dempsey, N. M.; Givord, D.; Reyne, G.; Dumas-Bouchiat, F. Autonomous Micro-Magnet Based Systems for Highly Efficient Magnetic Separation. *Appl. Phys. Lett.* **2011**. *99*, 232504.

[15] Pivetal, J.; Royet, D.; Ciuta, G.; Frenea-Robin, M.; Haddour, N.; Dempsey, N. M.; Dumas-Bouchiat, F.; Simonet, P. Micro-magnet Arrays for Specific Single Bacterial Cell Positioning. *J. Magn. Magn. Mater.* **2015**, *380*, 72-77.

[16] Godoy, M.; Moreno, A. J.; Jorge, G. A.; Ferrari, H. J.; Antonel, P. S.; Mietta, J. L.; Ruiz, M.; Negri, R. M.; Pettinari, M. J.; Bekeris, V. Micrometric Periodic Assembly of Magnetotactic Bacteria and Magnetic Nanoparticles Using Audio Tapes. *J. Appl. Phys.* **2012**, *111*, 044905.

[17] Gooneratne, C. P.; Kodzius, R.; Li, F.; Foulds, I.; Kosel, J. On-Chip Magnetic Bead Manipulation and Detection Using a Magnetoresistive Sensor-Based Micro-Chip: Design Considerations and Experimental Characterization. *Sensors* **2016**, *16*, 1369.

[18] Yassine, O.; Gooneratne, C. P.; Smara, D. A.; Li, F.; Mohammed, H.; Merzaban, J.; Kosel, J. Isolation of Cells for Selective Treatment and Analysis Using a Magnetic Microfluidic Chip. *Biomicrofluidics* **2014**, *8*, 034114.

[19] Li, F.; Kosel, J. An Efficient Biosensor Made of an Electromagnetic Trap and a Magneto-resistive Sensor. *Biosens. Bioelectron.* **2014**, *59*, 145-150.

[20] *Magnetic Nano- and Microwires*; Vazques, M. Ed.; Elsevier: US, **2015**.

[21] Ivanov, Y. P.; Alfadhel, A.; Alnassar, M.; Perez, J. E.; Vazquez, M.; Chuvilin, A.; Kosel, J. Tunable Magnetic Nanowires for Biomedical and Harsh Environment Applications. *Sci. Rep.* **2016**, *6*, 24189.

[22] Ivanov, Y. P.; Chuvilin, A.; Vivas, L. G.; Kosel, J.; Chubykalo-Fesenko, O.; Vázquez, M. Single Crystalline Cylindrical Nanowires – Toward Dense 3D Arrays of Magnetic Vortices. *Sci. Rep.* **2016**, *6*, 23844.

[23] Bran, C.; Ivanov, Yu. P.; Kosel, J.; Chubykalo-Fesenko, O.; Vazquez, M. Co/Au Multisegmented Nanowires: a 3D Array of Magnetostatically Coupled Nanopillars. *Nanotechnology* **2017**, *28*, 095709.

[24] Perez, J. E.; Ravasi, T.; Kosel, J. Mesenchymal Stem Cells Cultured on Magnetic Nanowire Substrates. *Nanotechnology* **2017**, *28*, 055703.

[25] Park, J. J.; Reddy, K. S. M.; Stadler, B.; Flatau, A. Magnetostrictive Fe–Ga/Cu Nanowires Array With GMR Sensor for Sensing Applied Pressure. *IEEE Sens. J.* **2017**, *17*, 2015-2020.

[26] Ivanov, Y. P.; Chuvilin, A.; Lopatin, S.; Kosel, J. Modulated Magnetic Nanowires for Controlling Domain Wall Motion: Toward 3D Magnetic Memories. *ACS Nano* **2016**, *10*, 5326-5332.

[27] Ivanov, Y. P.; Chuvilin, A.; Lopatin, S.; Mohammed, H.; Kosel, J. Direct Observation of Current-Induced Motion of a 3D Vortex Domain Wall in Cylindrical Nanowires. *ACS Appl. Mater. Interfaces* **2017**, *9*, 16741-16744.

[28] Vock, S.; Sasvári, Z.; Bran, C.; Rhein, F.; Wolff, U.; Kiselev, N.S.; Bogdanov, A.N.; Schultz, L.; Hellwig, O.; Neu, V. Quantitative Magnetic Force Microscopy Study of the Diameter Evolution of Bubble Domains in a Co/Pd Multilayer. *IEEE Trans. Magn.* **2011**, *47*, 2352-2355.

[29] Mitin, D.; Grobis, M.; Albrecht. M. Scanning Magnetoresistive Microscopy: An Advanced Characterization Tool for Magnetic Nanosystems. *Rec. Sci. Instrum.* **2016**, *87*, 023703.

[30] Shaw, G.; Kramer, R. B. G.; Dempsey, N. M.; Hasselbach, K. A Scanning Hall Probe Microscope for High Resolution, Large Area, Variable Height Magnetic Field Imaging. *Rec. Sci. Instrum.* **2016**, *87*, 113702.

[31] Schirhagl, R.; Chang, K.; Loretz, M.; Degen, C.L. Nitrogen-Vacancy Centers in Diamond: Nanoscale Sensors for Physics and Biology. *Annu. Rev. Phys. Chem*. **2014**. *65*, 83–105.

[32] Rodríguez, L.A.; Bran, C.; Reyes, D.; Berganza, E.; Vázquez, M.; Gatel, C.; Snoeck, E.; Asenjo, A. Quantitative Nanoscale Magnetic Study of Isolated Diameter-Modulated FeCoCu Nanowires. *ACS Nano* **2016**, *10*, 9669-9678;

[33] Wolf, D.; Rodriguez, L.A.; Béché, A.; Javon, E.; Serrano, L.; Magen, C.; Gatel, C.; Lubk, A.; Lichte, H.; Bals, S.; Van Tendeloo, G.; Fernández-Pacheco, A.; De Teresa, J.M.; Snoeck, E. 3D Magnetic Induction Maps of Nanoscale Materials Revealed by Electron Holographic Tomography. *Chem. Mater.* **2015**, *27*, 6771-6778.

[34] Biziere, N.; Gatel, C.; Lassalle-Balier, R.; Clochard, M.C.; Wegrowe, J.E.; Snoeck, E. Imaging the Fine Structure of a Magnetic Domain Wall in a Ni Nanocylinder. *Nano Lett.* **2013**, *13*, 2053-2057.

[35] Snoeck, E.; Dunin-Borkowski, R. E.; Dumestre, F.; Renaud, P.; Amiens, C.; Chaudret, B.; Zurcher P. Quantitative Magnetization Measurements on Nanometer Ferromagnetic Cobalt Wires Using Electron Holography. *Appl. Phys. Lett.* **2003**, *82*, 88-90.

[36] Akhtari-Zavareh, A.; Carignan, L. P.; Yelon, A.; Ménard, D.; Kasama, T.; Herring, R.; Dunin-Borkowski, R. E., McCartney, M. R.; Kavanagh, K. L. Off-Axis Electron Holography of Ferromagnetic Multilayer Nanowires. *J. Appl. Phys.* **2014**, *116*, 023902.

[37] Reyes, D.; Biziere, N.; Warot-Fonrose, B.; Wade, T.; Gatel, C. Magnetic Configurations in Co/Cu Multilayered Nanowires: Evidence of Structural and Magnetic Interplay. *Nano Lett.* **2016**, *16,* 1230–1236

[38] Ortega, E.; Santiago, U.; Giuliani, J.G.; Monton, C.; Ponce, A. In-situ Magnetization/Heating Electron Holography to Study the Magnetic Ordering in Arrays of Nickel Metallic Nanowires. *AIP Adv.* **2018**, *8*, 056813.

[39] Lopatin, S.; Ivanov, Y. P.; Kosel, J.; Chuvilin, A. Multiscale Differential Phase Contrast Analysis with a Unitary Detector. *Ultramicroscopy*, **2016**, *162*, 74-81.

[40] Qiu, Z. Q.; Bader, S. D. Surface Magneto-Optic Kerr Effect. *Rev. Sci. Instrum.* **2000**, *71*, 1243-1255.

[41] Vavassori, P. Polarization Modulation Technique for Magneto-Optical Quantitative Vector Magnetometry. *Appl. Phys. Lett.* **2000**, *77*, 1605-1607.

[42] Verduci, T.; Rufo, C.; Berger, A.; Metlushko, V.; Ilic, B.; Vavassori, P. Fourier Magnetic Imaging. *Appl. Phys. Lett.* **2011**, *99*, 092501.

[43] Nikulina, E.; Idigoras, O.; Vavassori, P.; Chuvilin, A.; Berger, A. Magneto-Optical Magnetometry of Individual 30 nm Cobalt Nanowires Grown by Electron Beam Induced Deposition. *Appl. Phys. Lett.* **2012**, *100*, 142401.

[44] Ivanov, Y. P.; Trabada, D. G.; Chuvilin, A.; Kosel, J.; Chubykalo-Fesenko, O.; Vázquez, M. Crystallographically Driven Magnetic Behaviour of Arrays of Monocrystalline Co Nanowires. *Nanotechnology* **2014**, *25*, 475702.

[45] Alnassar, M. Y.; Ivanov, Y. P.; Kosel, J. Flexible Magnetoelectric Nanocomposites with Tunable Properties. *Adv. Electron. Mater.* **2016**, *2*, 1600081.

[46] Giannuzzi, L. A.; Stevie, F. A. A Review of Focused Ion Beam Milling Techniques for TEM Specimen Preparation. *Micron* **1999**, *30*, 197–204.

[47] Vansteenkiste, A.; Leliaert, J.; Dvornik, M.; Helsen, M.; Garcia-Sanchez, F.; Van Waeyenberge, B. The Design and Verification of MuMax3. *AIP Adv.* **2014**. *4*, 107133.

[48] Leliaert, J.; Dvornik, M.; Mulkers, J.; De Clerc, J.; Milosevic, M. V.; Van Waeyenberge, B. Fast Micromagnetic Simulations on GPU—Recent Advances Made with mumax3. *J. Phys. D: Appl. Phys.* **2018**, *51*, 123002.

[49] Coey, J. M. D. *Magnetism and Magnetic Materials*; Cambridge Univ. Press: UK, **2010**.

[50] Yang, W.; Lambeth, D. N.; Laughlin, D. E. Dependence of Co Anisotropy Constants on Temperature, Processing, and Underlayer. *J. Appl. Phys.* **2000**, *87*, 6884-6886.

[51] *Handbook of Advanced Magnetic Materials: Vol 1. Nanostructural Effects*; Liu, Y.; Sellmyer, D. J.; Shindo D., Eds.; Springer: USA, **2006**.

[52] De La Torre Medina, J.; Darques, M.; Piraux, L. Strong Low Temperature Magnetoelastic Effects in Template Grown Ni Nanowires. *J. Phys. D: Appl. Phys.* **2008**, *41* 032008.

[53] Piraux, L.; Hamoir, G.; Encinas, A.; De La Torre Medina, J.; Araujo, F. A. Influence of the Packing Fraction and Host Matrix on the Magnetoelastic Anisotropy in Ni Nanowire Composite Arrays. *J. Appl. Phys.* **2013**, *114*, 123907.

[54] Leliaert, J.; Mulkers, J.; De Clercq, J.; Coene, A.; Dvornik, M.; Van Waeyenberge, B.. Adaptively Time Stepping the Stochastic Landau-Lifshitz-Gilbert Equation at Nonzero Temperature: Implementation and Validation in MuMax3. *AIP Adv.* **2017**, *7*, 125010.

[55] Leliaert, J.; Van de Wiele, B.; Vansteenkiste, A.; Laurson, L.; Durin, G.; Dupré, L.; Van Waeyenberge, B. A Numerical Approach to Incorporate Intrinsic Material Defects in Micromagnetic Simulations. *J. Appl. Phys.* **2014**, *115*, 17D102.

[56] Vidal, E. V.; Ivanov, Y. P.; Mohammed, H.; Kosel, J. A Detailed Study of Magnetization Reversal in Individual Ni Nanowires. *Appl. Phys. Lett.* **2015**, *106*, 032403.

[57] Ivanov, Y. P.; Vivas, L. G.; Asenjo, A.; Chuvilin, A.; Chubykalo-Fesenko, O.; Vazquez, M. Magnetic Structure of a Single-Crystal hcp Electrodeposited Cobalt Nanowire. *Europhys. Lett.* **2013**, *102*, 17009.

[58] Ivanov, Yu. P.; Vázquez, M.; Chubykalo-Fesenko, O. Magnetic Reversal Modes in Cylindrical Nanowires. *J. Phys. D: Appl. Phys.* **2013***, 46,* 485001.

Table of Contents Graphic.